Qin et al. *Zool. Res.* 2026, 47(1): 41−57
https://doi.org/10.24272/j.issn.2095-8137.2025.237
https://cstr.cn/32248.14.zr.2025.237

ZR | Zoological Research

Article Open Access

GPX3 improves endometrial receptivity by inhibiting ferroptosis via the Nrf2/GPX4 signaling pathway in sows

Xue Qin[1], Yi-Wen Sha[1], Xiao-Lin Wang[1], Zhen-Heng Lai[1], Yi Zheng[1], Rui Cai[1], Wei-Jun Pang[1,*]

[1] *Key Laboratory of Northwest China's Pig Breeding and Reproduction*, *Ministry of Agriculture and Rural Affairs P.R. China*, *College of Animal Science and Technology*, *Northwest A & F University*, *Yangling*, *Shaanxi* 712100, *China*

ABSTRACT

Obesity represents a major contributor to reproductive dysfunction during early mammalian pregnancy, yet the underlying mechanisms by which it impairs endometrial receptivity remain largely unknown. Through integrative metabolomic and transcriptomic profiling of uterine tissues from obese and control sows on gestational day 13, glutathione peroxidase 3 (GPX3) was identified as a key molecular determinant of endometrial receptivity. GPX3 expression was markedly reduced in the uterine tissue of obese sows and was closely associated with impaired receptivity. Functionally, GPX3 knockdown induced mitochondrial dysfunction, perturbed lipid peroxidation homeostasis, and triggered ferroptosis, ultimately reducing endometrial receptivity in palmitic acid (PA)-induced porcine endometrial epithelial cells (PEECs). In contrast, GPX3 overexpression restored mitochondrial function and suppressed ferroptotic signaling. Mechanistically, GPX3 deficiency activated ferroptosis via inhibition of the nuclear factor erythroid 2-related factor 2 (Nrf2)/GPX4 axis. Consistent with these findings, high-fat diet (HFD)-induced obese female mice exhibited reduced endometrial receptivity, down-regulation of the GPX3/Nrf2/GPX4 cascade, and mitochondrial ultrastructural damage. Overall, these findings establish GPX3 as a pivotal regulator of endometrial receptivity through modulation of Nrf2/GPX4-dependent ferroptotic signaling, providing novel insights into obesity-associated reproductive disorders.

Keywords: Obesity; GPX3; Endometrial receptivity; Nrf2/GPX4; Sow

INTRODUCTION

Obesity in sows is strongly associated with metabolic dysregulation, diminished steroidogenic capacity (Cools et al., 2013; Muro et al., 2023; Roongsitthichai & Tummaruk, 2014), and elevated oxidative stress (Zhang et al., 2024; Zhou et al., 2019), all of which contribute to reduced reproductive efficiency. Notably, obese sows show a 22% reduction in viable embryo numbers by gestational day 21 relative to counterparts with normal body condition, despite comparable ovulation rates (Gonzalez-Añover et al., 2011). In addition, high-producing sows with backfat thickness exceeding 23 mm display reduced litter weight gain and elevated piglet mortality (Li et al., 2023; Zhou et al., 2018), suggesting a potential link between excessive adiposity and reproductive impairment. However, the molecular mechanisms underlying these phenotypes remain insufficiently defined. Successful implantation depends on tightly regulated interactions between the trophoblast and uterine luminal epithelium. The implantation period is the most critical stage of pregnancy, during which approximately 40% of embryonic losses occur in pigs (Almeida & Dias, 2022; Qin et al., 2025). Emerging evidence suggests that obesity disrupts uterine receptivity by impairing the window of implantation (WOI), a hormonally regulated period of maternal-embryo communication (Qin et al., 2025). This disruption appears to be linked to metabolic disturbances that compromise the expression of endometrial receptivity markers (Bazzano et al., 2021; Bellver et al., 2021; Brewer & Balen, 2010; Yang et al., 2022), although the precise mechanisms remain unclear.

Obesity-induced metabolic disorders impair antioxidant defense capacity in sows (Jones, 2008; Muro et al., 2020), leading to sustained oxidative stress. Elevated reactive oxygen species (ROS) levels, together with decreased superoxide dismutase (SOD) and catalase (CAT) activity, have been documented in obese sows. Furthermore, malondialdehyde (MDA), a byproduct of lipid peroxidation (LPO) (Guo et al., 2022; Zhou et al., 2019), is positively correlated with backfat thickness. Heightened oxidative stress not only activates the NF-κB signaling cascade, thereby suppressing genes essential for endometrial receptivity, but also interferes with mitochondrial energy metabolism via oxidative damage to mitochondrial DNA. These events collectively impair adhesion between the embryonic

Received: 11 August 2025; Accepted: 01 September 2025; Online: 02 September 2025

Foundation items: This work was supported by the China Agriculture Research System (CARS-35-PIG), National Key Research and Development Program of China (2021YFF1000602) , and Key Research and Development Program of Shaanxi Province (2022ZDLNY01–04)

*Corresponding author, E-mail: pwj1226@nwafu.edu.cn

trophoblast and uterine epithelium (Deluao et al., 2022; Guerby et al., 2021; Hussain et al., 2021; Luo et al., 2019). Within the antioxidant defense system, the glutathione peroxidase (GPX) family plays a crucial role in reducing hydrogen peroxide (H_2O_2) and lipid hydroperoxides to preserve redox homeostasis (McMillan et al., 2022). Among the eight known GPX isoforms, GPX3 is a secretory antioxidant enzyme abundantly present in plasma and extracellular fluids and is expressed in the endometrium (Hauffe et al., 2020; Herault et al., 2012; Lipecki et al., 2022). GPX3 has been shown to attenuate ROS accumulation during decidualization and is significantly up-regulated during this process (Xu et al., 2014; Yao et al., 2021). However, the impact of obesity on uterine GPX3 expression and its role in regulating endometrial receptivity remain largely unknown.

To address this knowledge gap, this study employed integrated metabolomic and transcriptomic analyses of uterine tissues from obese and control sows, identifying GPX3 as a critical regulator of endometrial receptivity. Functional investigations demonstrated that GPX3 down-regulation impaired mitochondrial function, activated ferroptosis, and suppressed the Nrf2/GPX4 signaling axis, thereby compromising receptivity in sows. These findings uncover a mechanistic link between obesity-driven oxidative stress and uterine dysfunction during early gestation, offering novel insights into the pathogenesis of obesity-related reproductive disorders.

MATERIALS AND METHODS

Animals

All animal procedures were approved by the Institutional Animal Care and Use Committee (Approval Nos. IACUC2023-1101 and IACUC2024-0702) and conducted in accordance with established ethical guidelines. Third-parity crossbred sows (Large White×Landrace), aged approximately 2–2.5 years and weighing 190–240 kg, were sourced from Xinjiang Tiankang Breeding (China) and slaughtered at Pingao Food (China). Sows were grouped based on backfat thickness into a normal condition group (*n*=6) and an obese group (*n*=6) using visual body condition scores (Li et al., 2012; Qin et al., 2025), with matched parity and genetic background. All sows underwent double insemination and were sacrificed on day 13 post-insemination. After slaughter, the uterus was flushed with saline to confirm pregnancy via morphological assessment of elongated conceptuses. Backfat thickness and uterine weight were recorded, and both uterine tissues and uterine luminal fluids were collected. Blood was drawn from the antecubital vein, and serum was stored at −80°C. In addition, uterus samples were obtained from non-pregnant sows and from sows at gestational day 25 at the Animal Experiment Center of Northwest A&F University. Samples were snap-frozen in liquid nitrogen and stored at −80°C.

For mouse models, 8-week-old female ICR mice (22 g) were obtained from Chengdu Yaokang Biotechnology (China). Mice were provided *ad libitum* access to either a control diet (*n*=6, Cat# GB14924.3: 12.7% energy from fat) or a high-fat diet (*n*=6, Cat# H10060: 60% energy from fat) for 3 months, resulting in a final body weight of 60–70 g in the HFD group. Mice were housed under standard conditions at the Animal Breeding Center of Northwest A&F University. Male breeders were maintained on a control diet. Mating was confirmed by vaginal plug observation, and gestational day 0.5 was designated. On gestational day 5.5, female mice were anesthetized and administered 1% Evan's blue dye (CAS No. 2610-05-1 C8679, Sigma, USA) dissolved in physiological saline via tail vein injection. Mice were sacrificed at 2 h post-injection, and uterus, liver, adipose tissue, and serum samples were collected. Embryonic implantation sites were recorded.

Cell culture

Porcine endometrial epithelial cells (PEECs) were purchased from Weijia Technology (China) and maintained in Primed-icell-001 medium (China) at 37°C in a humidified 5% CO_2 atmosphere. Cells were cultured in 100 mm dishes and passaged into 6-, 12-, 24-, or 96-well plates upon reaching 80–90% confluence. For experimental treatment, 40 μmol/L palmitic acid (PA; P0500, Sigma, USA) was prepared in serum-free medium as described previously (Joshi-Barve et al., 2007; Listenberger et al., 2003; Wang et al., 2024) and applied for 48 h (PA group). For inhibition assays, cells were pretreated for 24 h with either the Nrf2 antagonist ML385 (CAS No.: HY-100523, MCE, USA) or the GPX4 inhibitor ML162 (CAS No.: HY-100002, MCE, USA), followed by co-incubation with PA and the respective inhibitor according to experimental design.

Enzyme-linked immunosorbent assay (ELISA)

Ferrous iron (Fe^{2+}) levels were quantified in serum (*n*=5) and uterine tissues (*n*=6) from sows, as well as in samples from mice (*n*=3) and cultured cells (*n*=3) using a Ferrous Iron Colorimetric Assay Kit (E-BC-K773-M; Wuhan Elabscience Biological Technology, China). Total antioxidant capacity (T-AOC) (*n*=6) (A015-2-1 96T), glutathione (GSH) (*n*=6) (A006-2-1 96T), MDA (*n*=6) (A003-1-2), and LPO (sows *n*=6, mice *n*=3) (A106-2) levels were assessed in uterine tissues and cells using commercial assays kits (Nanjing Jiancheng Bioengineering Institute, China).

Wound healing assay

Cells were cultured in 6-well plates to 90%–100% confluence. A sterile 200 μL pipette tip was used to generate uniform scratches in the monolayers. Detached cells were removed by washing with phosphate-buffered saline (PBS). Wound closure was recorded at 0, 6, 12, 24, and 36 h post-scratch using microscopy (*n*=3). Scratch width was quantified using ImageJ software. Migration rate was calculated as (initial wound width−wound width at observation)/interval time.

Oil Red O staining

Mouse uterine and liver tissues were fixed in 4% paraformaldehyde for 24 h, embedded in OCT compound, and cryosectioned at 8 μm thickness. Sections were stained with filtered 0.5% Oil Red O (diluted in 60% isopropanol) for 15 min at room temperature, differentiated in 60% isopropanol, counterstained with Mayer's hematoxylin, and mounted in glycerol gelatin. Lipid droplet size and area were evaluated microscopically (Olympus, Japan).

Hematoxylin and eosin (H&E) staining analysis

Adipose tissues (*n*=3) were fixed, embedded in paraffin, and sectioned at 4 μm using a rotary microtome. Sections were deparaffinized, rehydrated, stained with H&E, and visualized by light microscopy (IX73; Olympus, Japan).

RNA extraction and reverse transcription

Total RNA was extracted from uterine tissues and cells using TRIzol reagent (Invitrogen, USA), following previously described protocols (Qin et al., 2025). RNA purity was

confirmed by OD260/OD280 ratios and RNA concentration was measured using a spectrophotometer (Thermo Fisher Scientific, USA). Reverse transcription was performed using the R323-01 Kit (Vazyme, China) for subsequent analysis.

Quantitative real-time polymerase chain reaction (qPCR)

Primers were designed using Primer5 software and verified for specificity via melt curve analysis. All primer pairs spanned exon boundaries to prevent amplification of genomic DNA. qPCR was performed using 2×SYBR Green qPCR Master Mix (Q311-02, Vazyma, China) with the StepOnePlus Real-Time PCR System. The thermal profile was as follows: 95°C for 10 min, followed by 40 cycles at 95°C for 15 s and 60°C for 1 min (Zhang et al., 2025). Target gene expression was normalized to β-actin and GAPDH using the $2^{-\Delta\Delta Ct}$ method. PCR efficiencies ranged from 90% to 110%, and standard curve slopes were between −3.0 and −3.6. Negative controls included No Template Control (NTC). Primer sequences used in this experiment are provided in Supplementary Table S1.

Western blotting

PEECs and uterine tissues were lysed in RIPA buffer containing protease (1:100) and phosphatase inhibitors (1:100) (M7528, Lihe Biology, China).Protein samples (25 μg) were resolved by sodium dodecyl sulfate-polyacrylamide gel electrophoresis (SDS-PAGE) using 10% gels under the following electrophoresis conditions: 80 V for 20 min followed by 120 V for 1 h. Proteins were transferred to PVDF membranes (IPVH0010, Chennuo Biology, China) via wet transfer. Membranes were incubated overnight at 4 °C with primary antibodies, followed by 1 h incubation at room temperature with appropriate secondary antibodies. Band intensities were analyzed for gray values using ImageJ software, and protein expression levels were normalized to β-actin (*n*=3/4). Antibodies used are listed in Supplementary Table S2.

Small interfering RNA (siRNA) knockdown experiments

Gene silencing was performed in 6-well plates using Lipofectamine RNAiMAX (Invitrogen, USA) following the manufacturer's protocols. Cells were transfected with siRNA targeting GPX3 (siGPX3; Tong Yong, China) and control siRNA (Tong Yong, China). Lipofectamine RNAiMAX was diluted in Opti‑MEM (Invitrogen, USA) and mixed with siRNA before application. After 12 h of transfection, the medium was replaced with complete medium containing fetal bovine serum (FBS) to improve cell survival. Knockdown efficiency was assessed by RT-qPCR.

Immunofluorescence analysis

Immunofluorescence was used to detect GPX3, GPX4, and VEGFA expression in PEECs, and GPX3, GPX4, and PR expression in mouse uterine tissues. Samples were incubated with primary antibodies overnight at 4°C, followed by secondary antibodies for 2 h. Nuclei were counterstained with 4',6-diamidino-2-phenylindole (DAPI; Solarbio, China) for 15 min. Imaging was performed by fluorescence microscopy, and fluorescence intensities were quantified using ImageJ (*n*=3 per group). Negative controls included no primary antibody to exclude non-specific binding. Antibody details are provided in Supplementary Table S2.

Infrared thermography

Body surface temperature of freely moving mice was recorded during the light phase using an infrared camera (FLIR Systems, USA). Images were captured at room temperature while mice moved freely on a wire cage lid. Thermal data were analyzed using FLIR Tools software (*n*=4 biological replicates).

RNA sequencing (RNA-seq) and data analysis

Total RNA was extracted from uterine tissues of obese and control sows (*n*=4) using TRIzol reagent (Invitrogen, USA) and treated with DNaseI to remove genomic DNA contamination. RNA integrity was assessed using an Agilent Bioanalyzer. RNA libraries were prepared using the Illumina TruSeq Kit (USA) and sequenced on the Illumina HIseq2000 platform (paired-end reads, USA). Quality control was performed using FastQC, and Trimmomatic was used to trim adapters and filter low-quality sequences. Differential gene expression analysis was conducted using DESeq2. Gene Ontology (GO) and Kyoto Encyclopedia of Genes and Genomes (KEGG) enrichment analyses were performed to identify biological processes associated with differentially expressed genes (DEGs). KEGG pathway enrichment was based on unadjusted *P*-values<0.05. For volcano plots, adjusted *P*-values were used to control the false discovery rate (FDR). Genes were defined as significantly differentially expressed if $-\log_{10}$ (*P*-value) was greater than 1 and $\log_2$ fold change ($\log_2$FC) exceeded 1 or was less than −1. All bioinformatic analyses were conducted in R.

Liquid chromatography-tandem mass spectrometry (LC-MS/MS) metabolomics

Uterine tissues (100 mg) and uterine fluid samples (100 μL) from obese and control sows were homogenized in liquid nitrogen. Homogenates were resuspended in pre-cooled 80% methanol, vortexed thoroughly, incubated on ice for 5 min, and centrifuged at 15 000 ×*g* and 4°C for 20 min. A portion of the supernatant was diluted with LC-MS-grade water to a final concentration of 53% methanol, transferred to fresh Eppendorf (EP) tubes, and centrifuged again under the same conditions. The resulting supernatant was subjected to LC-MS/MS analysis. Metabolite annotation was performed using the KEGG (https://www.genome.jp/kegg/pathway.html), HMDB (https://hmdb.ca/ metabolites), and LIPIDMaps (http://www.lipidmaps.org/) databases. Multivariate statistical analyses, including principal component analysis (PCA) and partial least squares discriminant analysis (PLS-DA), were conducted using MetaX. Univariate analysis (*t*-test) was applied to determine statistical significance. Differential metabolites were defined by variable importance in projection (VIP) scores >1, *P*-values<0.05, and fold changes (FC) ≥2 or ≤0.5. Volcano plots were generated using ggplot2 in R based on $\log_2$(fold change) and $-\log_{10}$(*P*-value). Clustering heatmaps were created using z-score normalized intensity values of differential metabolites via the Pheatmap package in R.

Immunohistochemistry

Uterine tissues from sows and mice (*n*=3) were fixed in 4% paraformaldehyde for 24 h, embedded in paraffin, and sectioned at 4 μm thickness. Sections were deparaffinized, rehydrated, and subjected to antigen retrieval using citrate buffer (pH 6.0) under high-pressure heating at 121°C for 15 min. Endogenous peroxidase activity was quenched with 3% H_2O_2, followed by blocking with 5% bovine serum albumin (BSA) at room temperature for 1 h. Sections were incubated overnight at 4°C with primary anti-GPX3 antibody (1:200 dilution), washed with PBS, and then incubated with

horseradish peroxidase (HRP)-conjugated secondary antibody (1:500) for 1 h at room temperature. Visualization was achieved using a standardized 30 s diaminobenzidine (DAB) chromogenic reaction, followed by hematoxylin counterstaining, dehydration, and neutral resin mounting. GPX3-positive signals (brown granules) were visualized under a light microscope. Negative controls were processed identically except for substitution of the primary antibody with PBS.

Transmission electron microscopy (TEM)

Uterine tissues from sows and mice, as well as cell samples, were fixed in 2.5% glutaraldehyde/4% paraformaldehyde (0.1 mol/L phosphate buffer, pH 7.4) at 4°C for 24 h, post-fixed with 1% osmium tetroxide for 2 h, dehydrated through graded ethanol and acetone, infiltrated with epoxy resin, and polymerized at 60°C for 48 h. Ultrathin sections (70 nm) were cut using a Leica UC7 ultramicrotome, stained with uranyl acetate and lead citrate, and examined under a JEOL JEM-1400Flash TEM at 80 kV (n=3). Mitochondrial ultrastructure, including cristae integrity, matrix density, and membrane continuity, was assessed.

Scanning electron microscopy (SEM)

To assess pinopode morphology, uterine horns from pregnant sows (13 d) and pregnant mice (5.5 d) were dissected to expose the endometrial surface. Tissues were rinsed with saline and fixed in 2.5% glutaraldehyde, followed by triple PBS washes and fixation in 1% osmium tetroxide for 90 min. After washing, tissue blocks (3 mm^2) were dehydrated through a graded alcohol series and 100% acetone, dried, and plated with palladium for 30 s using an ion sputtering instrument (MSP-2S; IXRF Systems, USA). Three randomly selected areas per sample were imaged using SEM (GeminiSEM 500; Zeiss, Germany) to evaluate pinopode structure (n=3).

ROS detection

Endometrial epithelial cells were incubated with 10 μmol/L DCFH-DA (Beyotime Reactive Oxygen Species Assay Kit, S0033S, China) in serum-free medium at 37°C for 30 min. Following incubation, cells were washed with PBS, and fluorescence intensity (excitation/emission: 488/525 nm) was assessed via fluorescence microscopy (Nikon Eclipse Ti, Japan) or flow cytometry (Becton, Dickinson and Company, USA). For positive controls, cells were pretreated with 100 μmol/L H_2O_2 for 1 h. ROS levels were quantified using ImageJ, expressed as fold change relative to controls (n=3).

JC-1 mitochondrial membrane potential assay

Mitochondrial membrane potential was assessed using a JC-1 assay kit (C1071S, Beyotime, China). Endometrial epithelial cells were incubated with 5 μmol/L JC-1 dye at 37 °C for 30 min, washed twice with PBS, and analyzed by fluorescence microscopy (Nikon Eclipse Ti, Japan) or flow cytometry (Becton, Dickinson and Company, USA). Red fluorescence (JC-1 aggregates, Ex/Em 585/590 nm) and green fluorescence (JC-1 monomers, Ex/Em 514/529 nm) were measured, and the red/green ratio was used as an indicator of mitochondrial membrane potential. Cells treated with 10 μmol/L carbonyl cyanide m-chlorophenyl hydrazone (CCCP) for 1 h served as depolarization controls. Measurements from three independent experiments (n=3 replicates per group) were normalized to the control group.

For extended detection, after 24 h of treatment, cells were washed twice with PBS and harvested by trypsinization (1×10^5–6×10^5 cells). Cells were resuspended in 0.5 mL of culture medium and mixed with 0.5 mL of JC-1 staining solution by gentle inversion, followed by incubation at 37°C for 20 min. During staining, ice-cold 1×JC-1 buffer was prepared by diluting the 5×stock solution with distilled water. Post-incubation, cells were centrifuged at 600 ×g for 3–4 min at 4°C. The supernatant was discarded, and cells were washed twice with 1 mL of pre-chilled 1×JC-1 buffer, repeating centrifugation after each wash. Cells were finally resuspended in 1×JC-1 buffer and analyzed by flow cytometry (Nikon Eclipse Ti, Japan), with mitochondrial membrane potential quantified as the B2/B4 fluorescence ratio.

Statistical analysis

Statistical analyses were performed using SPSS v.26.0 and GraphPad Prism v.9.0. Two-group comparisons were conducted using Student's t-test. For comparisons among three or more groups, one-way or two-way analysis of variance (ANOVA) followed by Bonferroni's *post hoc* test were used. Normality was confirmed using the Shapiro-Wilk test. Results were expressed as mean±standard error of the mean (SEM), and all experiments were repeated independently at least three times. Statistical significance was defined as P<0.05.

RESULTS

Obesity impairs endometrial receptivity and down-regulates GPX3 expression in sows

Third-parity crossbred sows (Landrace×Yorkshire) were classified into normal (n=6) and obese (n=6) groups based on body condition scores (Qin et al., 2025). Uterine tissues and serum samples were collected on day 13 after two artificial inseminations, corresponding to the pre-implantation phase (Figure 1A). Serum biochemical analysis revealed significant increases in total cholesterol (CHO) (Figure 1B), triglycerides (TG) (Figure 1C), and low-density lipoprotein cholesterol (LDL-C) (Figure 1D) in obese sows, while high-density lipoprotein cholesterol (HDL-C) remained unchanged (Figure 1E), indicating disrupted lipid metabolism. Western blotting confirmed marked up-regulation of lipogenesis markers (FASN and FABP4) and down-regulation of lipolytic proteins (ATGL) in the obese group (Figure 1F, G). SEM of the endometrial surface revealed fewer microvilli, irregular depressions, and a flattened morphology in obese sows (Figure 1H), indicative of impaired endometrial receptivity (Lian et al., 2022; Ye et al., 2023). Integrated metabolomic and transcriptomic analyses showed clear separation between control and obese groups in PCA (Figure 1I; Supplementary Figure S1A), confirming data reliability. Metabolomic profiling revealed uterine metabolites included steroids and their derivatives (Supplementary Figure S1B), with differential metabolites primarily enriched in pentose phosphate and linoleic acid metabolism pathways (Supplementary Figure S1C, D), suggesting metabolic dysregulation in obese uteri. Uterine fluid metabolomics corroborated these findings. PCA and heatmap clustering demonstrated distinct separation between groups (Supplementary Figure S2A, B), with cavity fluid metabolites also enriched in steroid derivatives (Supplementary Figure S2C). Pathway analysis identified significant enrichment in adipokine signaling and PPAR signaling pathways (Supplementary Figure S2D, E), both critically involved in lipid metabolism regulation, further supporting disrupted uterine

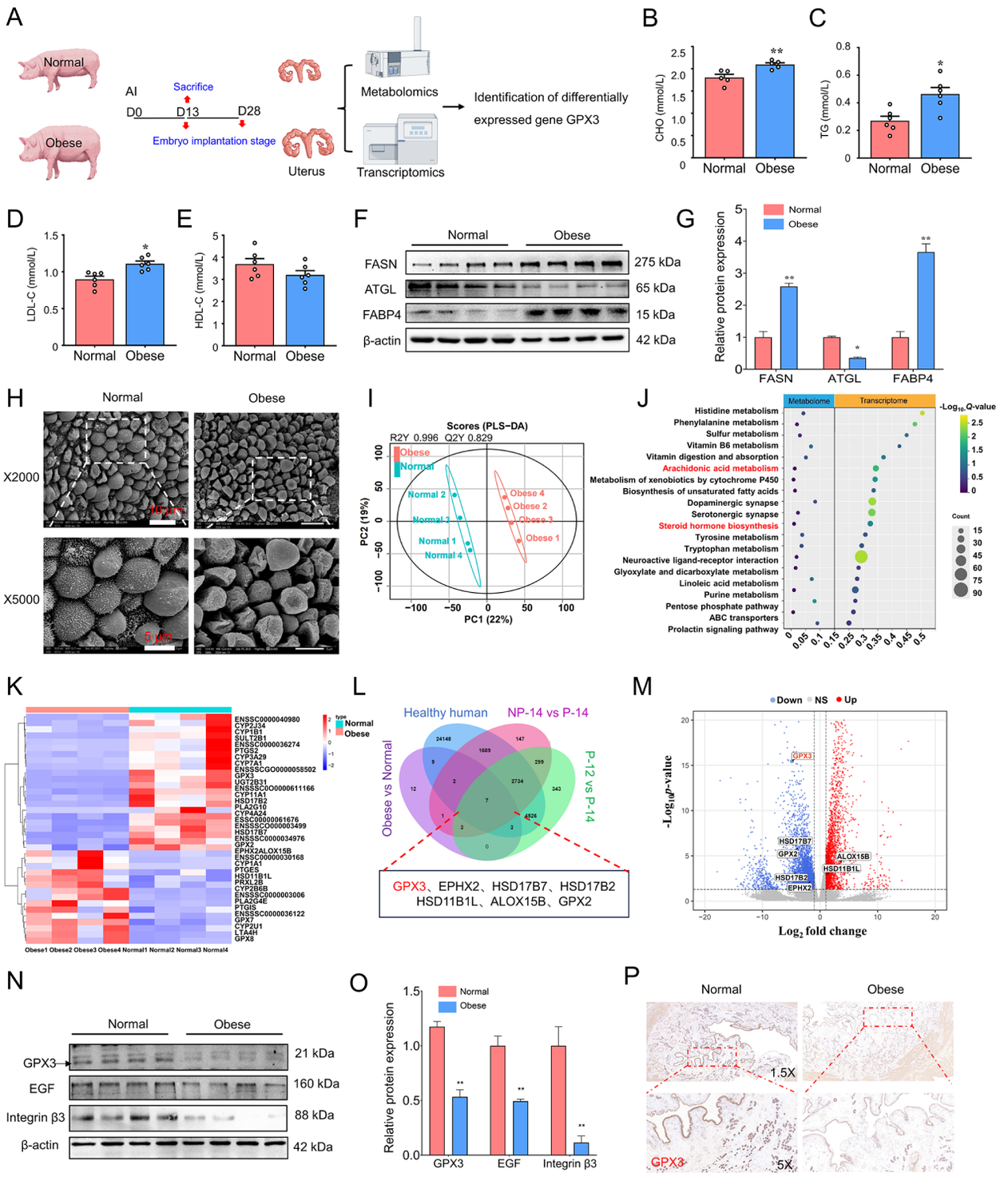

Figure 1 Obesity impairs endometrial receptivity and reduces GPX3 expression in sows

A: Uterine tissues collected from normal and obese sows on day 13 post-fertilization. B–E: Serum levels of total cholesterol (CHO), triglycerides (TG), low-density lipoprotein cholesterol (LDL-C), and high-density lipoprotein cholesterol (HDL-C) (*n*=6). F, G: Relative protein expression of FASN, ATGL, and FABP4 in uterine tissues (*n*=4). H: Scanning electron microscopy of pinopodes (scale bars=10 μm/5 μm) (*n*=3). I: Principal component analysis (PCA) of uterine metabolomics data (*n*=4). J, K: KEGG pathway enrichment and heatmap analyses integrating uterine metabolomics and RNA-seq data (*n*=4). L: Venn diagram comparing differentially expressed genes (DEGs) between Obese vs. Normal, Healthy human, NP-14 vs. P-14, and P-12 vs. P-14. M: Volcano plot comparing DEGs between Obese vs. Normal. N, NS: Not Significant. O: Relative protein expression levels of GPX3, EGF, and integrin β3 (*n*=4). P: Immunohistochemical staining of GPX3. *: $P<0.05$; **: $P<0.01$.

metabolic homeostasis in obesity. These findings confirmed that maternal obesity induces metabolic reprogramming of the uterine microenvironment at the metabolomic level, while highlighting potential mechanistic links between the obese sow phenotype and compromised endometrial receptivity. KEGG pathway enrichment integrating uterine metabolomic and transcriptomic data revealed co-enrichment of DEGs and differentially abundant metabolites (DAMs) in arachidonic acid

metabolism and steroid hormone biosynthesis pathways (Figure 1J), implicating obesity-driven lipid metabolic reprogramming in the disruption of embryo-implantation-related signaling. A total of 37 DEGs were functionally linked to these pathways (Figure 1K). Cross-species integration with human endometrial transcriptomes (GSE98386, *n*=40) and porcine datasets (non-pregnancy at 12 d (NP-12): GSM1185815; 12 d of pregnancy (P-12): GSM1185816; non-pregnancy at 14 d (NP-14): GSM1067874; and 14 d of pregnancy (P-14): GSM1067875) identified seven conserved genes (*GPX3*, *EPHX2*, *HSD17B7*, *HSD17B2*, *HSD11B1L*, *ALOX15B*, and *GPX2*; Figure 1L), with GPX3 exhibiting the most significant down-regulation in obese uterine tissues (Figure 1M). Western blotting confirmed reduced expression of endometrial receptivity markers alongside diminished GPX3 protein levels in obese uteri (Figure 1N, O). Immunohistochemistry and RT-qPCR further demonstrated decreased *GPX3* expression in both glandular epithelium and stromal compartments of obese endometrium (Figure 1P; Supplementary Figure S1E). Collectively, these results indicate that maternal obesity induces uterine lipid metabolic dysregulation, impairs endometrial receptivity, and suppresses GPX3 expression—suggesting a potential mechanistic link between GPX3-mediated oxidative stress imbalance and obesity-associated reproductive dysfunction.

GPX3 is dynamically up-regulated during early embryo implantation in sows

Gene-phenotype association analysis using the FarmGTEX database (https://pigbiobank.ipiginc.com/home) revealed a positive correlation between GPX3 expression and key reproductive traits in sows, including total litter size, number of health piglets born, total litter weight of live-born piglets, and backfat thickness (Figure 2A; Supplementary Figure S3A), suggesting a functional role for GPX3 in regulating sow fertility. Publicly available transcriptomic data further demonstrated stage-specific up-regulation of *GPX3* in uterine tissues during the implantation window, with significantly higher expression in the P-12 group compared to the NP-12 group, and further increases detected at P-14 (Figure 2B–D). To validate this temporal pattern, RT-qPCR was performed on uterine samples from non-pregnant (NP) sows, as well as those P-13 and P-25. *GPX3* mRNA levels peaked at P-13 and subsequently declined at P-25 (Figure 2E), mirroring the expression profiles of canonical endometrial receptivity markers *LIF* and *VEGFA* (Figure 2F, G). Western blotting confirmed synchronized up-regulation of GPX3 protein levels in P-13 uterine tissues, coinciding with elevated expression of receptivity-associated markers, including integrin β3, HOXA10, VEGFA, and LIF (Figure 2H, I). Together, these results indicate that GPX3 is tightly regulated in a pregnancy stage–dependent manner and orchestrates the expression of genes essential for endometrial receptivity. This temporal regulation suggests that GPX3 plays a critical role in defining the opening and closure of the implantation window in early pregnancy.

GPX3 enhances endometrial receptivity and promotes epithelial cell migration

To elucidate the molecular mechanisms by which lipid deposition impairs endometrial receptivity, a PA-induced lipid deposition model in PEECs was established using 40 μmol/L PA (Figure 3A). Successful induction of intracellular lipid accumulation was confirmed by Oil Red O staining, BODIPY, and western blotting, consistent with previous findings (Qin et al., 2025). Silencing GPX3 using siRNA (si-GPX3) achieved approximately 60% knockdown efficiency at the mRNA level (Figure 3B). Under both basal and PA-treated conditions, si-GPX3 significantly suppressed the mRNA expression of receptivity-associated genes *LIF* and *VEGFA* (Figure 3C, D). Western blotting further revealed concordant reductions in the protein levels of EGF, Integrin β3, HOXA10, and VEGFA following GPX3 knockdown (Figure 3E, F). Given the importance of epithelial migration during embryo implantation, wound healing assays demonstrated that GPX3 silencing impaired cell motility under both normal and PA-induced conditions (Figure 3G, H). Conversely, GPX3 overexpression (OE-GPX3) elevated transcript levels by approximately 30-fold (Figure 3I), significantly up-regulated *LIF* and *VEGFA* expression (Figure 3J, K), and increased the protein abundance of EGF, integrin β3, HOXA10, and LIF (Figure 3L, M). Enhanced migration was also observed in OE-GPX3 cells, as evidenced by accelerated wound closure (Figure 3N, O). Collectively, these findings demonstrate that GPX3 promotes endometrial receptivity by up-regulating implantation-related gene expression and facilitating epithelial cell migration, highlighting its critical role in endometrial functional remodeling.

GPX3 improves endometrial receptivity by preserving mitochondrial function in endometrial epithelial cells

TEM revealed pronounced mitochondrial swelling and vacuolization in endometrial epithelial cells from obese sows, in contrast with the intact mitochondrial ultrastructure observed in controls (Figure 4A), indicating that lipid dysmetabolism associated with obesity disrupts mitochondrial integrity. Based on these observations, the role of GPX3 in maintaining mitochondrial function was further examined to elucidate its mechanistic contribution to endometrial receptivity (Figure 4B). In PEECs co-treated with PA and si-GPX3, western blot analysis demonstrated marked suppression of key mitochondrial respiratory chain complexes, including ATP5A, UQCRC2, MTCO, and SDHB (Figure 4C, D). JC-1 staining coupled with flow cytometry demonstrated a significant reduction in mitochondrial membrane potential (ΔΨm) upon GPX3 knockdown, further exacerbated by PA exposure (Figure 4E–G). TEM analysis confirmed increased mitochondrial vacuolization and cristae fragmentation in the si-GPX3 groups (Figure 4H), demonstrating that GPX3 deficiency directly compromises both mitochondrial structure and function. In contrast, overexpression of GPX3 restored mitochondrial function. Protein levels of ATP5A, UQCRC2, MTCO, and SDHB were significantly up-regulated in OE-GPX3 cells (Figure 4I, J), and JC-1 assays revealed higher red/green fluorescence ratios, reflecting improved ΔΨm and partial rescue of PA-induced membrane damage (Figure 4K–M). TEM also validated reduced vacuolization and improved cristae morphology in the OE-GPX3 groups (Figure 4N). These findings demonstrate that GPX3 mitigates lipid accumulation-driven mitochondrial dysfunction by preserving respiratory complex expression, stabilizing ΔΨm, and protecting ultrastructural integrity, thereby contributing to enhanced endometrial receptivity.

GPX3 enhances endometrial receptivity and mitochondrial function by suppressing ferroptosis

Given the overlap between endometrial mitochondrial ultrastructural damage observed in the

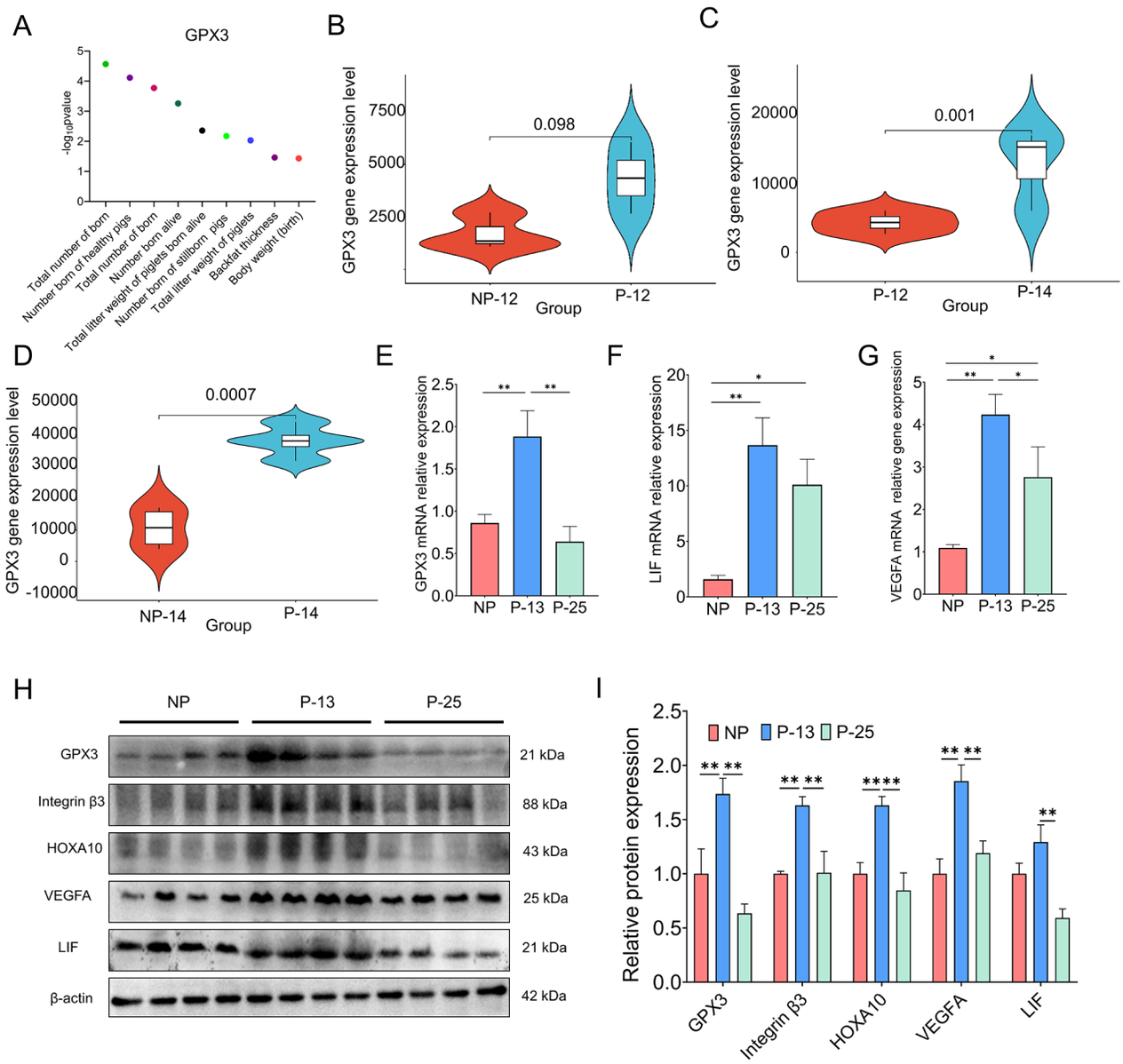

Figure 2 GPX3 is highly expressed during early embryo implantation in sows

A: Prediction of GPX3 association with reproductive performance based on PigBiobank data. B–D: Expression of GPX3 in NP-12 vs. P-12, P-12 vs. P-14, and NP-14 vs. P-14 (n=3). E–G: mRNA expression of GPX3, LIF, and VEGFA in NP, P-13, and P-25. H, I: Relative protein expression of GPX3, integrin β3, HOXA10, VEGFA, and LIF (n=4). NP: Non-pregnant, P-12: Pregnancy at 12 d, P-13: Pregnancy at 13 d, P-14: Pregnancy at 14 d, P-25: Pregnancy at 25. *: P<0.05; **: P<0.01.

endometrium—characterized by reduced membrane potential, cristae fragmentation, and vacuolization—and hallmark features of ferroptosis, we hypothesized that GPX3 regulates endometrial receptivity via modulation of ferroptotic signaling (Figure 5A). In obese sows, uterine tissue and serum exhibited elevated Fe^{2+} concentrations (Figure 5B, C), reduced T-AOC and GSH levels (Figure 5D, E), and increased MDA and LPO levels (Figure 5F, G), indicating a ferroptosis-prone microenvironment driven by iron overload and oxidative stress. Western blot analysis revealed significant down-regulation of GPX4, a key regulator of ferroptosis, in obese uteri (Figure 5H, I), suggesting a potential mechanistic link between GPX3 and ferroptotic regulation. To further investigate this, GPX3 was silenced in PEECs using siRNA. ROS assays demonstrated increased oxidative stress in the si-GPX3 group (Figure 5J, K), and ELISA confirmed elevated Fe^{2+} and depleted GSH concentrations (Figure 5L, M). Western blotting also showed reduced antioxidant protein expression (Supplementary Figure S4A, B) and RT-qPCR demonstrated suppressed *GPX4* mRNA levels following GPX3 knockdown (Figure 5N), collectively indicating that GPX3 deficiency promotes ferroptosis. Immunofluorescence assays confirmed co-localized downregulation of GPX4 and VEGFA in GPX3-silenced cells (Figure 5O), implicating disrupted ferroptosis defense and impaired receptivity. Conversely, GPX3 overexpression attenuated ROS generation (Figure 5P, Q), reduced intracellular Fe^{2+} accumulation (Figure 5R), restored GSH levels (Figure 5S), improved antioxidant capacity (Supplementary Figure S4C, D), and rescued *GPX4* mRNA expression (Figure 5T). Immunofluorescence further demonstrated OE-GPX3-driven up-regulation of GPX4 and VEGFA (Figure 5U). Together, these findings demonstrate

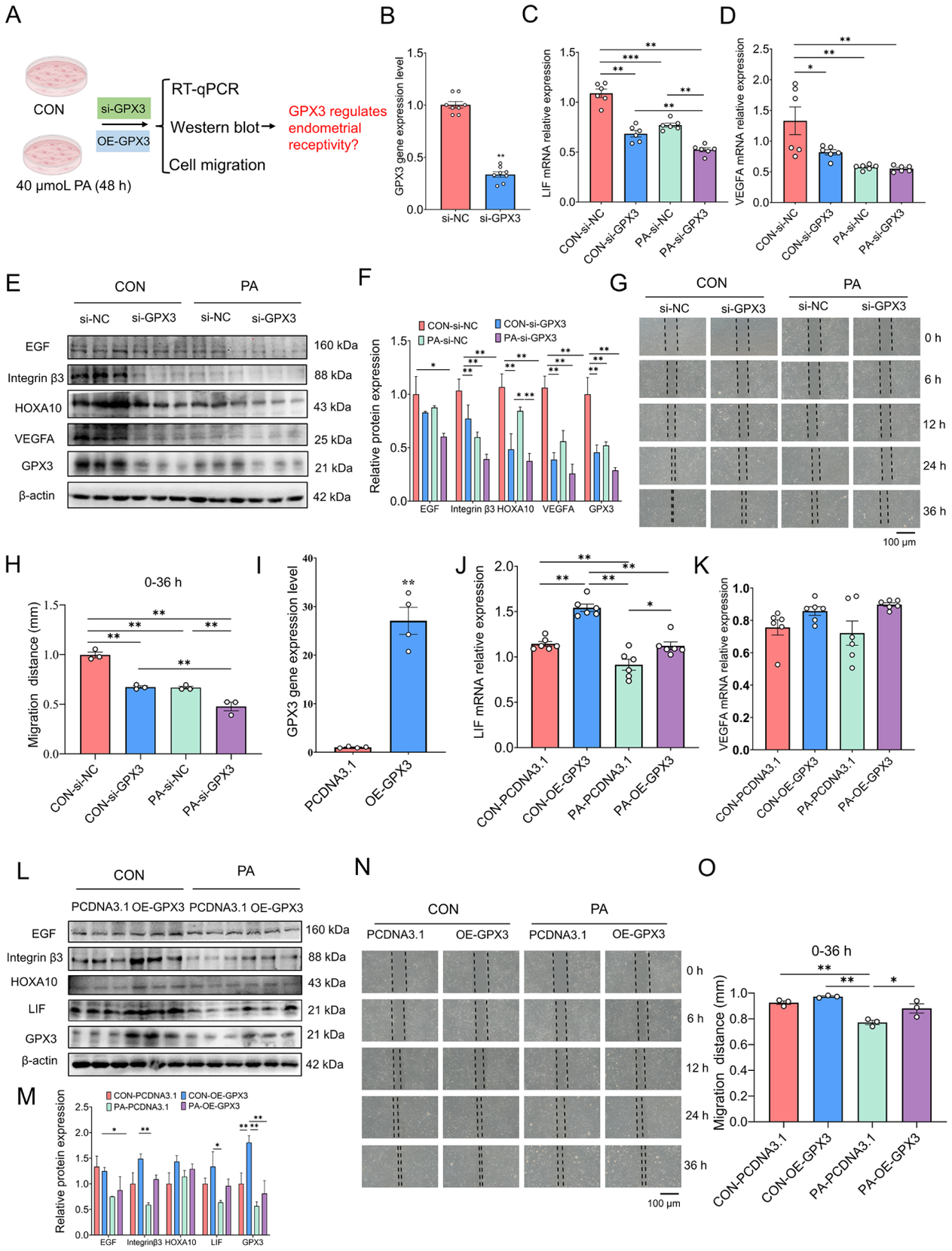

Figure 3 GPX3 enhances endometrial receptivity and promotes cell migration

A: Experimental groups treated with si-GPX3 and OE-GPX3. B: Interference efficiency of GPX3. C, D: mRNA expression of LIF and VEGFA. E, F: Relative protein expression of EGF, integrin β3, HOXA10, VEGFA, and GPX3 (*n*=3). G: Representative bright-field images showing PEEC migration at 0, 6, 12, 24, and 36 h (*n*=3). Scale bar: 100 μm. H: Quantification of wound closure rate. I: Overexpression efficiency of GPX3. J, K: mRNA expression of LIF and VEGFA. L, M: Relative protein expression of EGF, integrin β3, HOXA10, LIF, and GPX3 (*n*=3). N: Representative bright-field images showing PEEC migration at 0, 6, 12, 24, and 36 h (*n*=3). Scale bar: 100 μm. O: Quantification of wound closure rate. *: $P<0.05$; **: $P<0.01$.

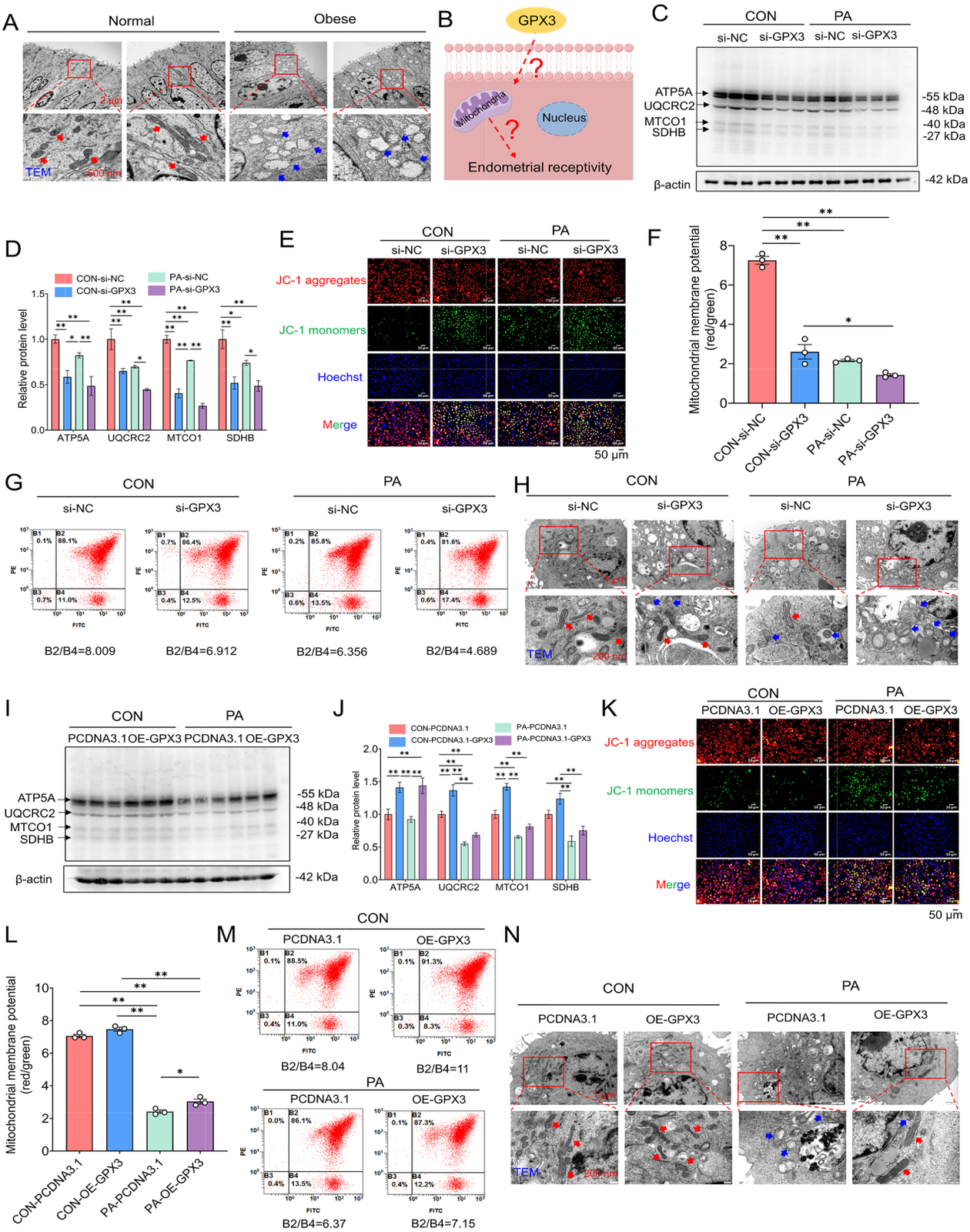

Figure 4 GPX3 enhances endometrial receptivity by improving mitochondrial function in endometrial epithelial cells

A: Scanning electron microscopy (SEM) images of mitochondria. B: Colocalization of GPX3 and mitochondria in PEECs. C, D: Relative protein expression of UQCRC2, ATP5A, MTCO1, and SDHB following GPX3 silencing (n=3). E, F: Mitochondrial membrane potential following GPX3 silencing (n=3). G: Flow cytometry assessment of mitochondrial membrane potential following GPX3 silencing (n=3). H: SEM images of mitochondria following GPX3 silencing (n=3). I, J: Relative protein expression of UQCRC2, ATP5A, MTCO1, and SDHB following GPX3 overexpression (n=3). K, L: Detection of mitochondrial membrane potential following GPX3 overexpression (n=3). M: Flow cytometry assessment of mitochondrial membrane potential following GPX3 overexpression (n=3). N: SEM images of mitochondria following GPX3 overexpression (n=3). *: P<0.05; **: P<0.01.

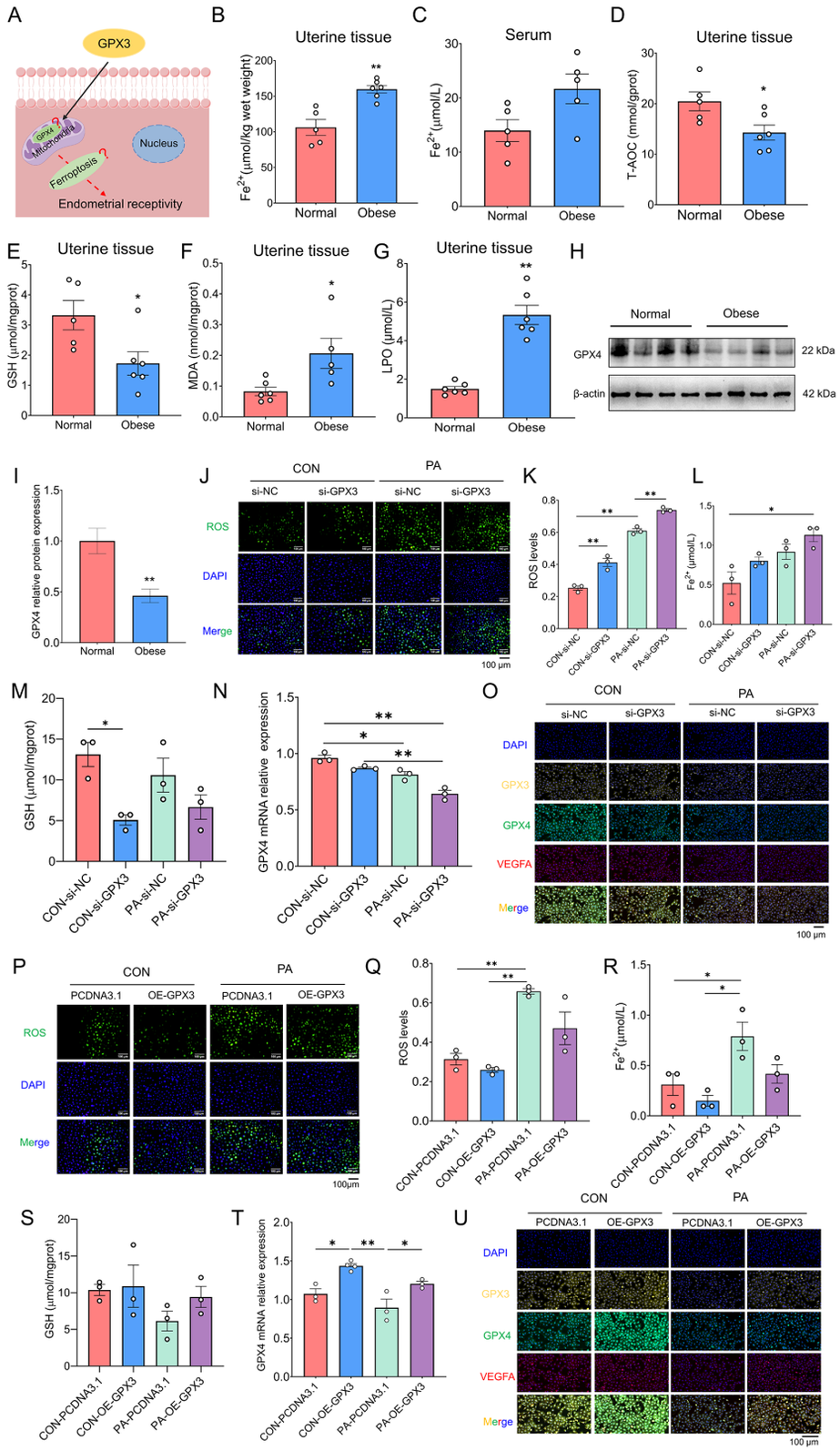

Figure 5 GPX3 enhances endometrial receptivity and mitochondrial function by suppressing ferroptosis

A: Schematic depiction of GPX3 involvement in ferroptosis regulation. B, C: Measurement of Fe^{2+} levels in uterine tissue (*n*=6) (B) and serum (*n*=5) (C) of sows. D, E: Total antioxidant capacity (T-AOC) (D) and GSH content (E) in sow uterine tissue. F, G: Quantification of MDA (F) and LPO (G) levels in uterine tissue (*n*=6). H, I: Relative protein expression of GPX4 in uterine tissue (*n*=4). J, K: Detection of ROS (green) following GPX3 silencing (*n*=3). Scale bar: 100 μm. L, M: Measurement of Fe^{2+} and GSH levels following GPX3 silencing (*n*=3). N: GPX4 mRNA expression following GPX3 silencing (*n*=3). O: Immunofluorescence staining of GPX3 (yellow), GPX4 (green), and VEGFA (red) following GPX3 silencing (*n*=3). Scale bar: 100 μm. P, Q: Detection of ROS (green) following GPX3 overexpression. Scale bar: 100 μm. (*n*=3). R, S: Fe^{2+} and GSH levels following GPX3 overexpression (*n*=3). T: GPX4 mRNA expression following GPX3 overexpression (*n*=3). U: Immunofluorescence staining of GPX3 (yellow), GPX4 (green), and VEGFA (red) following GPX3 overexpression (*n*=3). Scale bar: 100 μm. *: $P<0.05$; **: $P<0.01$.

that GPX3 inhibits lipid peroxidation-ferroptosis cascades by enhancing GPX4 expression, maintaining GSH homeostasis, and inhibiting Fe^{2+} overload, thereby promoting mitochondrial integrity and endometrial receptivity.

GPX3 inhibits ferroptosis in endometrial epithelial cells via activation of the Nrf2/GPX4 axis

Given the established role of Nrf2 in regulating iron homeostasis and inhibiting lipid peroxidation, we hypothesized that GPX3 modulates ferroptosis through activation of the Nrf2/GPX4 pathway (Figure 6A). Western blot analysis revealed that silencing GPX3 significantly down-regulated the protein expression of Nrf2, GPX4, and ferritin (Figure 6B, C). In contrast, GPX3 overexpression markedly up-regulated these proteins (Figure 6D, E), demonstrating bidirectional regulation of intracellular redox balance and iron sequestration via the Nrf2/GPX4 axis. To further determine whether ferroptosis acts downstream of GPX3, the GPX4-specific inhibitor ML162 (5 μmol/L) was applied (Figure 6F, G). Inhibition of GPX4 abrogated the protective effects of GPX3, evidenced by sustained Fe^{2+} accumulation and impaired GSH regeneration, leading to ferroptotic activation (Figure 6H, I). ML162 also suppressed the expression of genes associated with endometrial receptivity (Supplementary Figure S4E, F). Notably, ML162 blocked the GPX3 overexpression-induced up-regulation of endometrial receptivity-associated genes under both control and PA-treated conditions (Figure 6J, K), indicating that ferroptosis inhibition is essential for the pro-receptivity effects of GPX3. To verify the central role of Nrf2, the Nrf2-specific inhibitor ML385 (10 μmol/L) was employed, effectively reducing Nrf2 protein levels (Figure 6L, M). Under ML385 treatment, GPX3 failed to mitigate Fe^{2+} accumulation and could not restore GSH levels (Figure 6N, O). Moreover, ML385 completely abolished the GPX3-induced up-regulation of EGF, integrin β3, and HOXA10 (Figure 6P, Q), confirming that Nrf2 as an indispensable mediator of GPX3-driven enhancement of endometrial receptivity. Collectively, these findings establish that GPX3 exerts its anti-ferroptotic and pro-receptivity effects through Nrf2/GPX4 pathway activation.

HFD suppresses the GPX3/Nrf2/GPX4 axis, exacerbating endometrial ferroptosis and receptivity impairment

GPX3 amino acid sequences from mice, pigs, and humans were downloaded from the UniProt website (https://www.uniprot.org/) and aligned using MEGA v.11.0.13 and GeneDoc software (v.2.7.0.0). Homology analysis revealed high sequence conservation across species (Supplementary Figure S5A). To validate the functional relevance of these findings *in vivo*, an HFD-induced obesity model was established in mice. HFD-fed females exhibited significantly elevated mean body weight (60–65 g) compared to controls (Figure 7A), and infrared thermography indicated substantial metabolic dysregulation (Figure 7B). At gestational day 5.5, the number of implantation sites was markedly reduced in the HFD group (Figure 7C), suggesting impaired embryo implantation capacity resulting from lipid accumulation. Histological and molecular analyses confirmed pronounced lipid accumulation in the uterus, liver, and inguinal white adipose tissue (iWAT), as evidenced by Oil Red O and H&E staining and increased expression of adipogenic markers (FASN, FABP4, CEBPα) alongside reduced lipolysis (p-HSL/HSL ratio; Figure 7D–F), indicating a pro-lipogenic uterine microenvironment. SEM further demonstrated collapsed pinopodes and reduced microvilli density in the endometrial epithelium of HFD mice (Figure 7G). Endometrial receptivity-associated genes were significantly down-regulated, with both western blotting and immunohistochemistry confirming reduced GPX3 protein expression (Figure 7H–J), implicating GPX3 deficiency in impaired receptivity. To assess ferroptosis activation, ELISA assays showed elevated uterine Fe^{2+} and serum lipid peroxides in HFD mice (Figure 7K–M). TEM revealed swollen mitochondria with vacuolization and cristae disruption (Figure 7N), consistent with ferroptotic morphology observed in obese sows. Western blotting also demonstrated suppression of Nrf2 and GPX4 expression in HFD uterine tissues (Figure 7O, P), and immunofluorescence co-localization confirmed concurrent reduction of GPX3, GPX4, and PR intensities (Figure 7Q). Collectively, these findings demonstrate that HFD suppresses GPX3 expression and disrupts Nrf2/GPX4 axis activity, leading to iron overload, oxidative lipid damage, and mitochondrial dysfunction, thereby inducing ferroptosis and impairing endometrial receptivity.

DISCUSSION

This study identified GPX3 as a key regulator of obesity-induced impairment of endometrial receptivity in sows. Notably, the findings revealed for the first time that the GPX3/Nrf2/GPX4 signaling axis plays a central role in maintaining redox equilibrium and suppressing ferroptotic damage within the endometrium, thereby preserving endometrial receptivity under obesogenic conditions (Figure 8).

Obese sows displayed pronounced metabolic dysregulation in the uterine microenvironment, characterized by elevated levels of CHO, TG, and LDL-C, accompanied by up-regulated expression of lipogenesis-related genes and down-regulated expression of endometrial receptivity markers. These metabolic abnormalities parallel clinical observations demonstrating that elevated body mass index correlates with lower endometrial LIF concentrations and higher risk of recurrent pregnancy loss (Metwally et al., 2007, 2014). Histological analyses further confirmed the presence of structurally compromised pinopodes in both obese sows and HFD mouse models, characterized by reduced villus density, pinopode collapse, and ectopic lipid deposition. Such morphological disruptions likely reflect hormonally mediated dysfunction of uterine glandular epithelium, arising from altered estrogen-progesterone balance during early gestation (Leeners et al., 2017). Previous studies have shown that obesity disrupts progesterone secretion dynamics, including a reduction of up to 45% during early pregnancy due to insufficient luteal function (Muro et al., 2020), ultimately weakening maternal-embryo signaling. Similarly, in obese Iberian sows, gestational obesity has been shown to impair lipid homeostasis, elevating estrogen while lowering progesterone concentrations (Torres-Rovira et al., 2014). Obesity-induced systemic oxidative stress may also exacerbate uterine lipotoxicity via NADPH oxidase 2 (NOX2)-dependent pathways, thereby promoting abnormal accumulation of TG and non-esterified fatty acids (NEFA), inhibiting steroid hormone biosynthesis (Henriquez-Olguin et al., 2023; Hu et al., 2019; Joseph et al., 2019; Roberts et al., 2009), and contributing to structural degeneration of the endometrium and reduced implantation success. Additional obesity-related metabolic disorders, such as leptin resistance and insulin insensitivity, may also contribute to uterine dysfunction. Elevated circulating leptin, commonly observed in

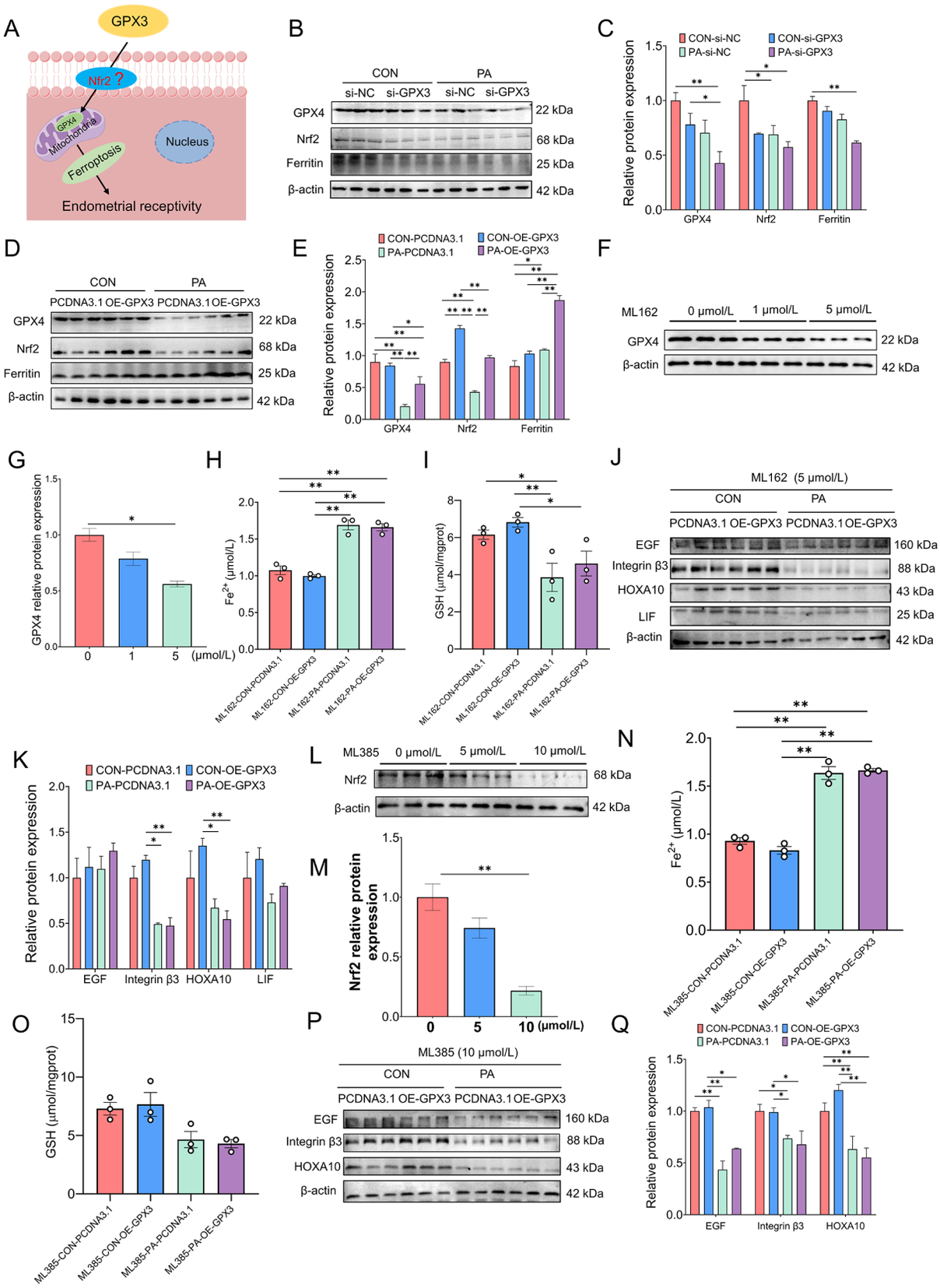

Figure 6 GPX3 suppresses endometrial epithelial cell ferroptosis via activation of the Nrf2/GPX4 axis

A: Schematic illustration of GPX3-mediated regulation of GPX4 and ferroptosis. B, C: Relative protein expression of GPX4, Nrf2, and ferritin following GPX3 silencing (n=3). D, E: Relative protein expression of GPX4, Nrf2, and ferritin following GPX3 overexpression (n=3). F, G: Relative protein expression of GPX4 (n=3). H: Detection of Fe^{2+} in PEECs. I: Detection of GSH in PEECs. J, K: Relative protein expression of EGF, integrin β3, HOXA10, and LIF (n=3). L, M: Relative protein expression of Nrf2 (n=3). N: Detection of Fe^{2+} in PEECs. O: Detection of GSH in PEECs. P, Q: Relative protein expression of EGF, integrin β3, HOXA10, and LIF (n=3). *: P<0.05; **: P<0.01.

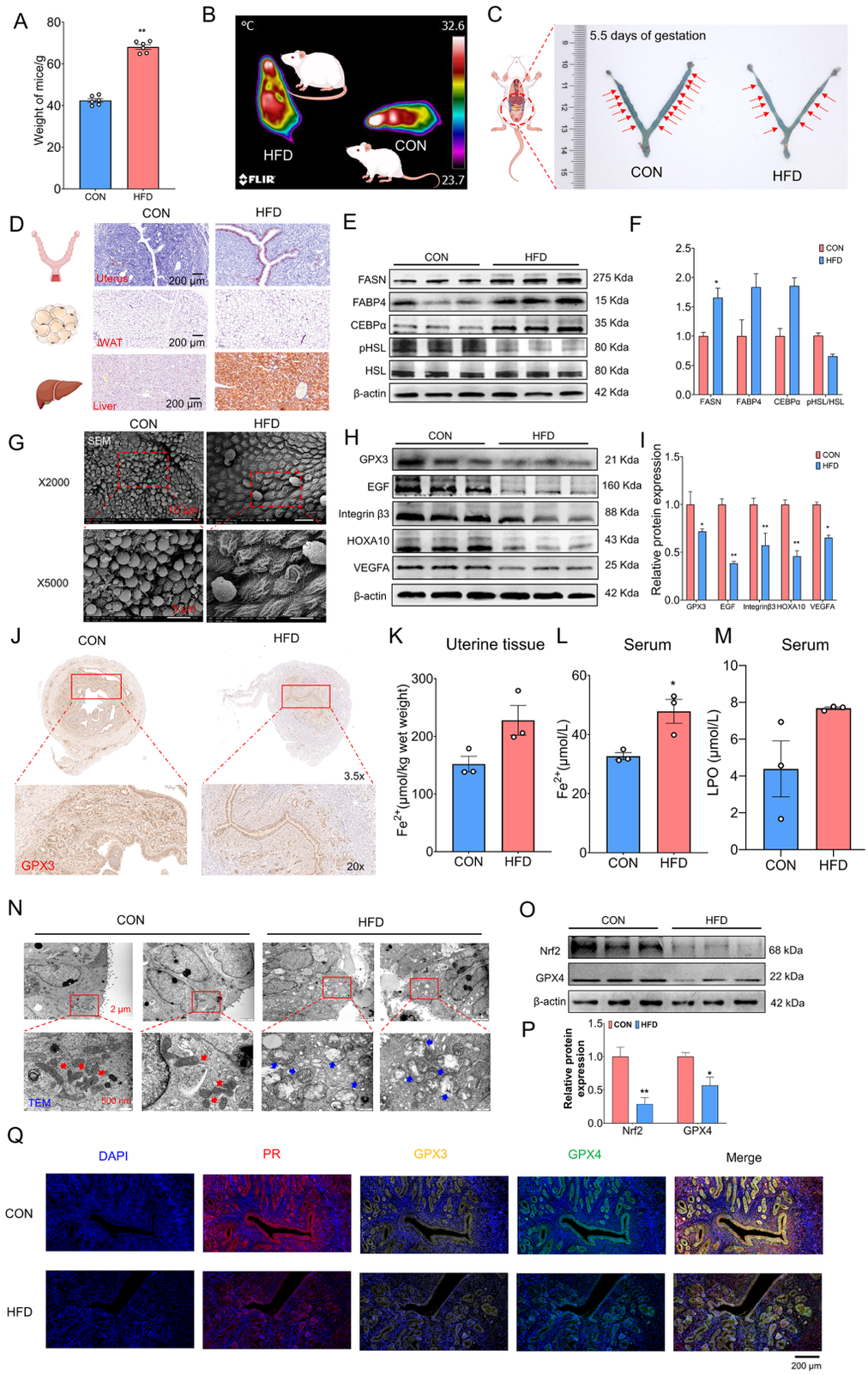

Figure 7 HFD-induced suppression of the GPX3/Nrf2/GPX4 axis exacerbates endometrial ferroptosis and impairs receptivity

A: Body weight changes in mice (*n*=6). B: Heat production and core body temperature changes in mice (*n*=4). C: Embryo implantation sites in each group (*n*=6). D: Representative images of Oil Red O staining in uterine and liver tissues, and H&E and Oil Red O staining in iWAT (scale bar =200 μm). E, F: Relative protein expression of FASN, FABP4, CEBPα, and pHSL/HSL (*n*=3). G: Scanning electron microscopy (SEM) images of pinopodes (scale bar=10 μm/5 μm) (*n*=3). H, I: Relative protein expression of GPX3, EGF, integrin β3, HOXA10, and VEGFA (*n*=3). J: Immunohistochemical staining of GPX3 in the uterus. K, L: Detection of Fe^{2+} in uterine tissue (K) and serum (L) (*n*=3). M: Detection of LPO in serum (*n*=3). N: SEM images of mitochondria (*n*=6). Scale bar: 200 μm. O, P: Relative protein expression of Nrf2 and GPX4. Q: Immunofluorescence staining of GPX3 (yellow), GPX4 (green), and PR (red) in uterus (*n*=3). Scale bar: 200 μm. *: P<0.05; **: P<0.01.

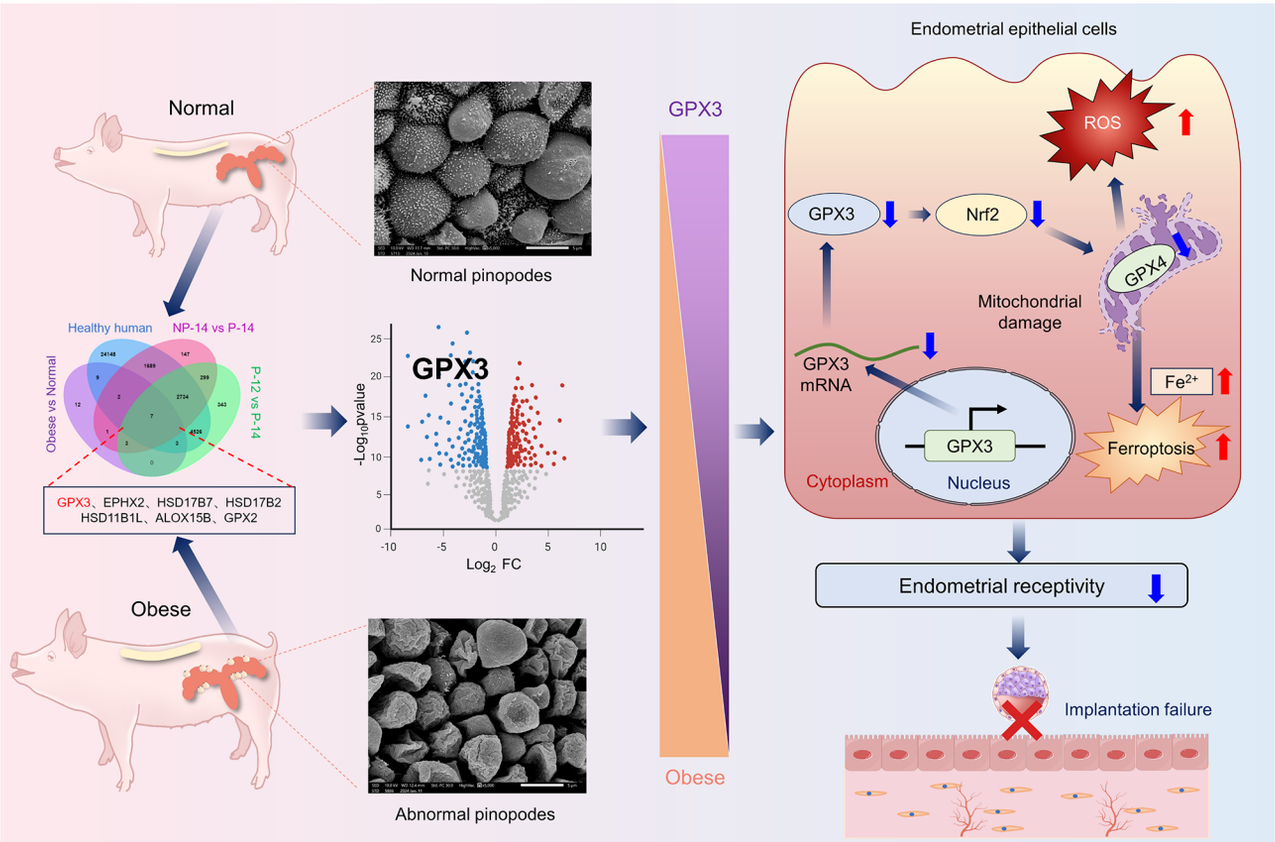

Figure 8 Schematic model illustrating the effect of GPX3 on endometrial receptivity and embryo implantation in obese sows

In obese sows, GPX3 down-regulation in uterine tissue inhibited the Nrf2/GPX4 axis, leading to ferroptosis activation, accompanied by mitochondrial damage and decreased endometrial receptivity. Scale bars: 5 μm for both SEM images.

obesity, suppresses the expression of genes involved in endometrial receptivity and impairs hormonal regulation of implantation-related pathways (Comninos et al., 2014; Lin et al., 2015; Neves et al., 2025; Ray et al., 2022; Yura et al., 2005). Compared to lean individuals, obese individuals consistently exhibit higher leptin levels and correspondingly lower endometrial competence (Gonzalez-Añover et al., 2011). Analysis of uterine fluid composition revealed a significant increase in fatty acid content in obese sows, with pathway enrichment implicating PPAR and lipid factor signaling pathways. These findings indicate that the microenvironment during maternal-fetal recognition may also be influenced by metabolic status (Zhang et al., 2017). Overall, these findings suggest that excess adiposity in sows leads to the release of free fatty acids from adipocytes, leading to lipid accumulation within the uterus and uterine fluid. This, in turn, disrupts lipid metabolism and redox homeostasis, culminating in ferroptosis, uterine structural degeneration, and impaired endometrial receptivity.

Integrated transcriptomic and metabolomic analyses revealed a previously unrecognized regulatory role for GPX3 in the disrupted uterine microenvironment associated with obesity. GPX3 expression was markedly reduced in uterine tissues from both obese sows and HFD-fed mice, in contrast to the robust expression observed in normal sows. In non-obese endometria, high GPX3 expression may contribute to the maintenance of redox homeostasis via exosome-mediated intercellular signaling. The mechanisms underlying GPX3 down-regulation under obesogenic conditions appear multifactorial. Epigenetic changes induced by obesity may inhibit GPX3 transcription or enzymatic activity (Nirgude & Choudhary, 2021), while increased oxidative burden and excessive lipid accumulation may accelerate GPX3 depletion and promote ROS production (Li et al., 2023). In addition, endocrine dysregulation—particularly altered progesterone secretion—may modulate GPX3 expression, consistent with reports demonstrating strong progesterone-mediated induction of GPX3 both *in vivo* and *in vitro* models (Yao et al., 2021). These findings align with prior observations indicating that GPX3 expression in subcutaneous white adipose tissue is significantly lower in obese individuals than in lean individuals, with more severe suppression in those with insulin resistance (Hauffe et al., 2020; Song et al., 2024). Dynamic increases in circulating GPX3 following bariatric surgery further support its involvement in systemic metabolic regulation (Iacoangeli et al., 2020; Langhardt et al., 2018). Notably, GPX3 expression in uterine tissues of obese sows and mice exhibited a significant positive correlation with key genes involved in endometrial receptivity. Moreover, temporal profiling during early gestation revealed a peak in GPX3 expression on day 13, coinciding with maximal expression of endometrial receptivity markers. These observations suggest that GPX3 may orchestrate transcriptional programs governing the implantation window. These findings are consistent with prior reports that GPX3 is selectively expressed in the decidualizing uterus between gestational days 5 and 8 but absent in pseudopregnant or delayed implantation states (Xu et al., 2014; Yao et al., 2021).To further verify the role of GPX3 in embryo implantation, targeted manipulation of GPX3 in PEECs demonstrated that GPX3 up-regulation enhanced the

expression of receptivity-associated genes and promoted migratory capacity, whereas GPX3 silencing exerted the opposite effect. Together, these findings indicate that temporally regulated GPX3 expression contributes to the precise molecular coordination required for embryo implantation, potentially determining the timing and competence of the receptive window.

Both obese sows and HFD-induced mice exhibited marked ultrastructural damage to endometrial mitochondria, characterized by swelling, disrupted cristae architecture, and extensive vacuolization. These morphological abnormalities prompted the hypothesis that reduced GPX3 expression under obesogenic conditions impairs endometrial function by compromising mitochondrial structure and function. This hypothesis was substantiated through *in vitro* analysis. Notably, GPX3 silencing in PEECs led to pronounced mitochondrial disorganization, including increased vacuolization and cristae disruption, accompanied by reductions in mitochondrial membrane potential and expression of respiratory chain complexes. Conversely, GPX3 overexpression mitigated mitochondrial damage induced by PA exposure, partially restoring mitochondrial integrity and function. These findings suggest that GPX3 acts as a core component of the mitochondrial antioxidant defense system in the uterine endometrium, maintaining mitochondrial homeostasis through redox regulation. Independent studies further support this interpretation. Previous proteomic profiling has revealed that obesity reduces the abundance of electron transport chain complexes and ATP synthase subunits in the mitochondrial inner membrane of endometrial tissues, impairing oxidative phosphorylation and decreasing ATP production (Fowden et al., 2021).Thus, GPX3 insufficiency may exacerbate mitochondrial dysfunction, amplifying endometrial disruption in the context of lipid overload. Studies have also linked GPX3 dysregulation to increased inflammatory signaling and oxidative stress in obese individuals, further implicating this enzyme in the pathophysiology of metabolic inflammation (Hauffe et al., 2020; Lee et al., 2008; Song et al., 2024). Consistently, in the PA-treated cellular model used in this study, GPX3 knockout increased oxidative stress and suppressed the expression of key antioxidant enzymes in endometrial epithelial cells. These findings collectively indicate that GPX3 exerts a pivotal role in maintaining mitochondrial redox stability and may mitigate obesity-induced uterine dysfunction by preserving mitochondrial integrity and metabolic competence.

This study identified a critical mechanistic link between GPX3 deficiency and ferroptosis-mediated disruption of endometrial receptivity under obesogenic conditions. Although mitochondria are known to modulate multiple forms of regulated cell death, the role of GPX3-dependent redox metabolism in controlling mitochondrial ferroptosis within the endometrium remains poorly defined. Analysis of uterine tissue from both obese sows and HFD-fed mice revealed hallmark features of ferroptosis, including decreased T-AOC, elevated levels of lipid peroxidation markers such as MDA and LPO, and impaired GSH metabolism. These alterations align with core ferroptotic mechanisms, including iron overload, membrane lipid peroxidation, and collapse of the antioxidant defense system (Hadian & Stockwell, 2020; Jiang et al., 2021). Functional perturbation experiments further supported this link. Notably, GPX3 knockdown in endometrial cells led to pronounced increases in ROS, accompanied by down-regulation of antioxidant enzymes GPX5, SOD1, and CAT, and marked reductions in GPX4 expression. These molecular changes also coincided with intracellular Fe^{2+} accumulation and increased lipid peroxidation.The observed GPX4 suppression is particularly relevant, given its essential role in detoxifying lipid hydroperoxides and maintaining endometrial redox stability. Prior studies have implicated GPX4 loss in impaired uterine receptivity and implantation failure (Huang et al., 2025; Li et al., 2021; Liang et al., 2023), with diminished GPX4 expression and increased lipid peroxidation also documented in women with recurrent implantation failure (Lu et al., 2024). Ferroptosis regulation involves multiple upstream transcription factors, including p53, NUPR1, and Nrf2 (Dodson et al., 2019; Jiang et al., 2015; Liu et al., 2021). Among these, Nrf2 functions as a master regulator of the antioxidant response, orchestrating the expression of genes such as GPX4 that mitigate ferroptotic stress by converting cytotoxic lipid hydroperoxides into inert lipid alcohols (Huang et al., 2025; Li et al., 2021; Liang et al., 2023). In the present study, GPX3 overexpression specifically activated the Nrf2/GPX4 signaling pathway, whereas pharmacologic inhibition of Nrf2 (ML385) or GPX4 (ML162) fully abrogated this effect. These findings confirm that the anti-ferroptotic function of GPX3 is mediated through the Nrf2/GPX4 axis. Overall, these results establish that obesity-associated GPX3 downregulation inhibits Nrf2/GPX4 signaling, exacerbates mitochondrial oxidative damage, and promotes ferroptotic cell death within the endometrium, ultimately compromising endometrial receptivity during early pregnancy.

This study has several limitations. It is unclear whether GPX3 modulates ferroptosis in endometrial cells exclusively via GPX4, or through additional downstream effectors. Additionally, all rescue experiments in this study employed chemical inhibitors, which may introduce off-target effects and confound mechanistic interpretations. Generation of uterus-specific GPX3 knockout mice would provide more definitive evidence for the role of GPX3 in regulating embryo implantation. In parallel, integration of single-cell methylation sequencing with uterine organoid models could enable systematic investigation of GPX3 involvement in the regulation of imprinted gene networks.

CONCLUSION

This study established a mechanistic link between obesity and uterine dysfunction, identifying GPX3 as a critical regulator of endometrial receptivity. GPX3 down-regulation induced ferroptosis in endometrial cells through suppression of Nrf2/GPX4 signaling, resulting in impaired receptivity. These findings provide insight into the pathogenesis of obesity-associated reproductive disorders and highlight GPX3 as a potential molecular target for therapeutic intervention.

DATA AVAILABILITY

Raw RNA-seq data generated in this study have been deposited in the Genome Sequence Archive (GSA) of the China National Center for Bioinformation (CRA028347) and in the National Center for Biotechnology Information (NCBI) (BioProjectID PRJNA1294545) (https://www.ncbi.nlm.nih.gov/sra/PRJNA1294545). Metabolomic datasets from uterine tissue and uterine cavity fluid are available via iProX (PXD066372) (https://www.iprox.cn/page/project.html?id=IPX0012713000). Science Data Bank (Transcriptomics DOI: 10.57760/sciencedb.j00139.00311; Metabolome of uterine tissue DOI: 10.57760/sciencedb.33237; Metabolome of uterine

cavity fluid DOI:10.57760/sciencedb.33240). Public transcriptomic data were obtained from GEO database (https://www.ncbi.nlm.nih.gov/gds), including healthy human endometrial samples (GSE98386, *n*=40) and sow uterine samples (non-pregnancy at 12 d (NP-12): GSM1185815; 12 d of pregnancy (P-12): GSM1185816; non-pregnancy at 14 d (NP-14): GSM1067874; and 14 d of pregnancy (P-14): GSM1067875).

SUPPLEMENTARY DATA

Supplementary data to this article can be found online.

COMPETING INTERESTS

The authors declare that they have no competing interests.

AUTHORS' CONTRIBUTIONS

X.Q. conceived the study. X.Q. and Y.W.S. performed the experiments. X.Q., Y.W.S., and X.L.W. analyzed the data. X.Q. and X.L.W wrote the manuscript. Z.H.L., Y.Z., R.C., and W.J.P. supervised the study. W.J.P. provided funding support. All authors read and approved the final version of the manuscript.

ACKNOWLEDGMENTS

The authors sincerely appreciate the samples provided by Xinjiang Tiankang Breeding Co., Ltd. (Gansu, China).

REFERENCES

Almeida FRCL, Dias ALNA. 2022. Pregnancy in pigs: the journey of an early life. *Domestic Animal Endocrinology*, **78**: 106656.

Bazzano MV, Sarrible GB, Berón de Astrada M, et al. 2021. Obesity modifies the implantation window and disrupts intrauterine embryo positioning in rats. *Reproduction*, **162**(1): 61–72.

Bellver J, Marín C, Lathi RB, et al. 2021. Obesity affects endometrial receptivity by displacing the window of implantation. *Reproductive Sciences*, **28**(11): 3171–3180.

Brewer CJ, Balen AH. 2010. The adverse effects of obesity on conception and implantation. *Reproduction*, **140**(3): 347–364.

Comninos AN, Jayasena CN, Dhillo WS. 2014. The relationship between gut and adipose hormones, and reproduction. *Human Reproduction Update*, **20**(2): 153–174.

Cools A, Maes D, Decaluwé R, et al. 2013. Peripartum changes in orexigenic and anorexigenic hormones in relation to back fat thickness and feeding strategy of sows. *Domestic Animal Endocrinology*, **45**(1): 22–27.

Deluao JC, Winstanley Y, Robker RL, et al. 2022. Oxidative stress and reproductive function: reactive oxygen species in the mammalian pre-implantation embryo. *Reproduction*, **164**(6): F95–F108.

Dodson M, Castro-Portuguez R, Zhang DD. 2019. NRF2 plays a critical role in mitigating lipid peroxidation and ferroptosis. *Redox Biology*, **23**: 101107.

Fowden AL, Camm EJ, Sferruzzi-Perri AN. 2021. Effects of maternal obesity on placental phenotype. *Current Vascular Pharmacology*, **19**(2): 113–131.

Gonzalez-Añover P, Encinas T, Torres-Rovira L, et al. 2011. Ovulation rate, embryo mortality and intrauterine growth retardation in obese swine with gene polymorphisms for leptin and melanocortin receptors. *Theriogenology*, **75**(1): 34–41.

Guerby P, Tasta O, Swiader A, et al. 2021. Role of oxidative stress in the dysfunction of the placental endothelial nitric oxide synthase in preeclampsia. *Redox Biology*, **40**: 101861.

Guo GL, Zhou TT, Ren FY, et al. 2022. Effect of maternal catalase supplementation on reproductive performance, antioxidant activity and mineral transport in sows and piglets. *Animals*, **12**(7): 828.

Hadian K, Stockwell BR. 2020. SnapShot: ferroptosis. *Cell*, **181**(5): 1188–1188. e1.

Hauffe R, Stein V, Chudoba C, et al. 2020. GPx3 dysregulation impacts adipose tissue insulin receptor expression and sensitivity. *JCI Insight*, **5**(11): e136283.

Henriquez-Olguin C, Meneses-Valdes R, Raun SH, et al. 2023. NOX2 deficiency exacerbates diet-induced obesity and impairs molecular training adaptations in skeletal muscle. *Redox Biology*, **65**: 102842.

Herault O, Hope KJ, Deneault E, et al. 2012. A role for GPx3 in activity of normal and leukemia stem cells. *The Journal of Experimental Medicine*, **209**(5): 895–901.

Hu CJ, Yang YY, Li JY, et al. 2019. Maternal diet-induced obesity compromises oxidative stress status and angiogenesis in the porcine placenta by upregulating Nox2 expression. *Oxidative Medicine and Cellular Longevity*, **2019**: 2481592.

Huang B, Wang H, Liu S, et al. 2025. Palmitoylation-dependent regulation of GPX4 suppresses ferroptosis. *Nature Communications*, **16**(1): 867.

Hussain T, Murtaza G, Metwally E, et al. 2021. The role of oxidative stress and antioxidant balance in pregnancy. *Mediators of Inflammation*, **2021**: 9962860.

Iacoangeli A, Lin T, Al Khleifat A, et al. 2020. Genome-wide meta-analysis finds the ACSL5-ZDHHC6 locus is associated with ALS and links weight loss to the disease genetics. *Cell Reports*, **33**(4): 108323.

Jiang L, Kon N, Li TY, et al. 2015. Ferroptosis as a p53-mediated activity during tumour suppression. *Nature*, **520**(7545): 57–62.

Jiang XJ, Stockwell BR, Conrad M. 2021. Ferroptosis: mechanisms, biology and role in disease. *Nature Reviews Molecular Cell Biology*, **22**(4): 266–282.

Jones DP. 2008. Radical-free biology of oxidative stress. *American Journal of Physiology-Cell Physiology*, **295**(4): C849–C868.

Joseph LC, Avula UMR, Wan EY, et al. 2019. Dietary saturated fat promotes arrhythmia by activating NOX2 (NADPH Oxidase 2). *Circulation: Arrhythmia and Electrophysiology*, **12**(11): e007573.

Joshi-Barve S, Barve SS, Amancherla K, et al. 2007. Palmitic acid induces production of proinflammatory cytokine interleukin-8 from hepatocytes. *Hepatology*, **46**(3): 823–830.

Langhardt J, Flehmig G, Klöting N, et al. 2018. Effects of weight loss on glutathione peroxidase 3 serum concentrations and adipose tissue expression in human obesity. *Obesity Facts*, **11**(6): 475–490.

Lee YS, Kim AY, Choi JW, et al. 2008. Dysregulation of adipose glutathione peroxidase 3 in obesity contributes to local and systemic oxidative stress. *Molecular Endocrinology*, **22**(9): 2176–2189.

Leeners B, Geary N, Tobler PN, et al. 2017. Ovarian hormones and obesity. *Human reproduction update*, **23**(3): 300–321.

Li L, Lu MZ, Peng YL, et al. 2023. Oxidatively stressed extracellular microenvironment drives fibroblast activation and kidney fibrosis. *Redox Biology*, **67**: 102868.

Li PC, Jiang MD, Li KT, et al. 2021. Glutathione peroxidase 4-regulated neutrophil ferroptosis induces systemic autoimmunity. *Nature Immunology*, **22**(9): 1107–1117.

Li YZ, Wang LH, Johnston LJ. 2012. Sorting by parity to reduce aggression toward first-parity sows in group-gestation housing systems. *Journal of Animal Science*, **90**(12): 4514–4522.

Lian WS, Gao DY, Huang C, et al. 2022. Heat stress impairs maternal endometrial integrity and results in embryo implantation failure by regulating transport-related gene expression in Tongcheng pigs. *Biomolecules*, **12**(3): 388.

Liang DG, Feng Y, Zandkarimi F, et al. 2023. Ferroptosis surveillance independent of GPX4 and differentially regulated by sex hormones. *Cell*, **186**(13): 2748–2764. e22.

Lin XH, Liu ME, Xu HY, et al. 2015. Leptin down-regulates γ-ENaC expression: a novel mechanism involved in low endometrial receptivity. *Fertility and Sterility*, **103**(1): 228–235. e3.

Lipecki J, Mitchell AE, Muter J, et al. 2022. EndoTime: non-categorical

timing estimates for luteal endometrium. *Human Reproduction*, **37**(4): 747–761.

Listenberger LL, Han XL, Lewis SE, et al. 2003. Triglyceride accumulation protects against fatty acid-induced lipotoxicity. *Proceedings of the National Academy of Sciences of the United States of America*, **100**(6): 3077–3082.

Liu J, Song XX, Kuang FM, et al. 2021. NUPR1 is a critical repressor of ferroptosis. *Nature Communications*, **12**(1): 647.

Lu Y, Shao Y, Cui W, et al. 2024. Excessive lipid peroxidation in uterine epithelium causes implantation failure and pregnancy loss. *Advanced Science (Weinh)*, **11**(4): e2302887.

Luo Z, Xu X, Sho T, et al. 2019. ROS-induced autophagy regulates porcine trophectoderm cell apoptosis, proliferation, and differentiation. *American Journal of Physiology-Cell Physiology*, **316**(2): C198–C209.

McMillan JDR, Sands KN, Cooney GS, et al. 2022. Unexpected formation and potent antioxidant activity of macrocyclic dimers containing disulfide and selenide groups. *Angewandte Chemie International Edition*, **61**(50): e202213744.

Metwally M, Preece R, Thomas J, et al. 2014. A proteomic analysis of the endometrium in obese and overweight women with recurrent miscarriage: preliminary evidence for an endometrial defect. *Reproductive Biology and Endocrinology*, **12**(1): 75.

Metwally M, Tuckerman EM, Laird SM, et al. 2007. Impact of high body mass index on endometrial morphology and function in the peri-implantation period in women with recurrent miscarriage. *Reproductive Biomedicine Online*, **14**(3): 328–334.

Muro BBD, Carnevale RF, Leal DF, et al. 2020. Supplemental progesterone during early pregnancy exerts divergent responses on embryonic characteristics in sows and gilts. *Animal*, **14**(6): 1234–1240.

Muro BBD, Carnevale RF, Leal DF, et al. 2023. The importance of optimal body condition to maximise reproductive health and perinatal outcomes in pigs. *Nutrition Research Reviews*, **36**(2): 351–371.

Neves D, Neto AC, Salazar M, et al. 2025. A narrative review about the intricate crosstalk among endometrium, adipose tissue, and neurons in endometriosis. The multifaceted role of leptin. *Obesity Reviews*, **26**(4): e13879.

Nirgude S, Choudhary B. 2021. Insights into the role of GPX3, a highly efficient plasma antioxidant, in cancer. *Biochemical Pharmacology*, **184**: 114365.

Qin X, Yang MH, Yu Y, et al. 2025. Melatonin improves endometrial receptivity and embryo implantation via MT2/PI3K/LIF signaling pathway in sows. *Journal of Animal Science and Biotechnology*, **16**(1): 4.

Ray I, Meira LB, Michael A, et al. 2022. Adipocytokines and disease progression in endometrial cancer: a systematic review. *Cancer and Metastasis Reviews*, **41**(1): 211–242.

Roberts VHJ, Smith J, McLea SA, et al. 2009. Effect of increasing maternal body mass index on oxidative and nitrative stress in the human placenta. *Placenta*, **30**(2): 169–175.

Roongsitthichai A, Tummaruk P. 2014. Importance of backfat thickness to reproductive performance in female pigs. *The Thai Journal of Veterinary Medicine*, **44**(2): 171–178.

Song YJ, Zhu MJ, Islam MA, et al. 2024. Glutathione peroxidase 3 is essential for countering senescence in adipose remodelling by maintaining mitochondrial homeostasis. *Redox Biology*, **77**: 103365.

Torres-Rovira L, Astiz S, Gonzalez-Añover P, et al. 2014. Intake of high saturated-fat diets disturbs steroidogenesis, lipid metabolism and development of obese-swine conceptuses from early-pregnancy stages. *The Journal of Steroid Biochemistry and Molecular Biology*, **139**: 130–137.

Wang Y, Gong JF, Heng N, et al. 2024. Melatonin alleviates palmitic acid-induced mitochondrial dysfunction by reducing oxidative stress and enhancing autophagy in bovine endometrial epithelial cells. *Journal of Animal Science and Biotechnology*, **15**(1): 108.

Xu X, Leng JY, Gao F, et al. 2014. Differential expression and anti-oxidant function of glutathione peroxidase 3 in mouse uterus during decidualization. *FEBS Letters*, **588**(9): 1580–1589.

Yang TL, Zhao J, Liu F, et al. 2022. Lipid metabolism and endometrial receptivity. *Human Reproduction Update*, **28**(6): 858–889.

Yao ST, Wei W, Cao R, et al. 2021. Resveratrol alleviates zea-induced decidualization disturbance in human endometrial stromal cells. *Ecotoxicology and Environmental Safety*, **207**: 111511.

Ye QH, Li HY, Xu BY, et al. 2023. Butyrate improves porcine endometrial epithelial cell receptivity via enhancing acetylation of histone H3K9. *Molecular Nutrition & Food Research*, **67**(16): 2200703.

Yura S, Itoh H, Sagawa N, et al. 2005. Role of premature leptin surge in obesity resulting from intrauterine undernutrition. *Cell Metabolism*, **1**(6): 371–378.

Zhang CXW, Candia AA, Sferruzzi-Perri AN. 2024. Placental inflammation, oxidative stress, and fetal outcomes in maternal obesity. *Trends in Endocrinology & Metabolism*, **35**(7): 638–647.

Zhang Y, Wang Q, Wang HM, et al. 2017. Uterine fluid in pregnancy: a biological and clinical outlook. *Trends in Molecular Medicine*, **23**(7): 604–614.

Zhang LT, Zhang T, Song XR, et al. 2025. CircSHOC2 regulates steroid hormone synthesis in ovarian granulosa cells through the mir-130b-5p/ASH1L pathway. *Zoological Research*, **46**(5): 1108–1120.

Zhou YF, Xu T, Cai AL, et al. 2018. Excessive backfat of sows at 109 d of gestation induces lipotoxic placental environment and is associated with declining reproductive performance. *Journal of Animal Science*, **96**(1): 250–257.

Zhou YF, Xu T, Wu YH, et al. 2019. Oxidative stress and inflammation in sows with excess backfat: up-regulated cytokine expression and elevated oxidative stress biomarkers in placenta. *Animals*, **9**(10): 796.